Preface for Applied Scanning Probe Methods Vol. XI–XIII

The extremely positive response by the advanced community to the Springer series on Applied Scanning Probe Methods I–X as well as intense engagement of the researchers working in the field of applied scanning probe techniques have led to three more volumes of this series. Following the previous concept, the chapters were focused on development of novel scanning probe microscopy techniques in Vol. XI, characterization, i.e. the application of scanning probes on various surfaces in Vol. XII, and the application of SPM probe to biomimetics and industrial applications in Vol. XIII. The three volumes will complement the previous volumes I–X, and this demonstrates the rapid development of the field since Vol. I was published in 2004. The purpose of the series is to provide scientific background to newcomers in the field as well as provide the expert in the field sound information about recent development on a worldwide basis.

Vol. XI contains contributions about recent developments in scanning probe microscopy techniques. The topics contain new concepts of high frequency dynamic SPM technique, the use of force microscope cantilever systems as sensors, ultrasonic force microscopy, nanomechanical and nanoindentation methods as well as dissipation effects in dynamic AFM, and mechanisms of atomic friction.

Vol. XII contains contributions of SPM applications on a variety of systems including biological systems for the measurement of receptor–ligand interaction, the imaging of chemical groups on living cells, and the imaging of chemical groups on live cells. These biological applications are complemented by nearfield optical microscopy in life science and adhesional friction measurements of polymers at the nanoscale using AFM. The probing of mechanical properties by indentation using AFM, as well as investigating the mechanical properties of nanocontacts, the measurement of viscous damping in confined liquids, and microtension tests using in situ AFM represent important contributions to the probing of mechanical properties of surfaces and materials. The atomic scale STM can be applied on heterogeneous semiconductor surfaces.

Vol. XIII, dealing with biomimetics and industrial applications, deals with a variety of unconventional applications such as the investigations of the epicuticular grease in potato beetle wings, mechanical properties of mollusc shells, electro-oxidative lithography for bottom-up nanofabrication, and the characterization of mechanical properties of biotool materials. The application of nanomechanics as tools for the investigation of blood clotting disease, the study of piezo-electric polymers, quantitative surface characterization, nanotribological characterization of

carbonaceous materials, and aging studies of lithium ion batteries are also presented in this volume.

We gratefully acknowledge the support of all authors representing leading scientists in academia and industry for the highly valuable contribution to Vols. XI–XIII. We also cordially thank the series editor Marion Hertel and her staff members Beate Siek and Joern Mohr from Springer for their continued support and the organizational work allowing us to get the contributions published in due time.

We sincerely hope that readers find these volumes to be scientifically stimulating and rewarding.

August 2008

Bharat Bhushan
Harald Fuchs

2 Atomic Force Microscope Cantilevers Used as Sensors for Monitoring Microdrop Evaporation

Elmar Bonaccurso · Dmytro S. Golovko · Paolo Bonanno · Roberto Raiteri · Thomas Haschke · Wolfgang Wiechert · Hans-Jürgen Butt

Abstract. For studying the evaporation of millimetre-sized drops of liquids techniques such as video-microscope imaging and ultra-precision weighing with electronic microbalances or with quartz crystal microbalances have been employed in the past decades. Similar techniques are, however, hardly applicable to microscopic drops. Moreover, they do not provide a measure of the interfacial stresses arising at the contact area between liquid and solid. Here we demonstrate the use of atomic force microscope (AFM) cantilevers as sensitive stress, mass, and temperature sensors for monitoring the evaporation of microdrops of water from solid surfaces. Starting from considerations on drops in equilibrium, we will further discuss evaporating drops and details of the experimental technique. We will show how the evaporation of water microdrops on a hydrophobic surface differs from the evaporation on a hydrophilic surface, and how this difference becomes more pronounced towards the end of evaporation. We further show that one-side metal-coated cantilevers, acting as bimetals, allow measuring the average temperature of an evaporating microdrop. Finally, we will discuss two further applications of microdrops evaporating on cantilevers, namely testing the local cleanliness of cantilevers' surfaces and calibrating cantilevers' spring constants.

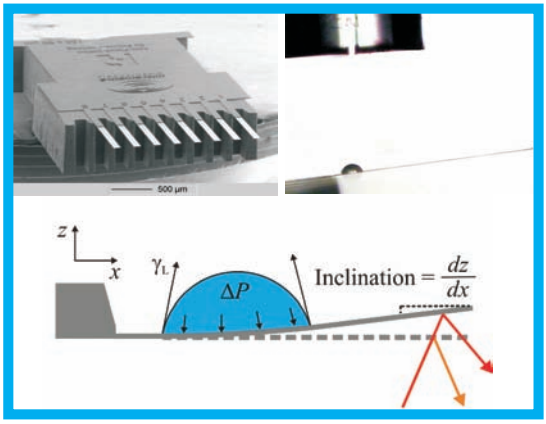

Key words: Microdrop evaporation, Evaporation law, Atomic force microscopy, Micromechanical cantilevers, Surface tension, Young's equation, Vaporization heat, Spring constant calibration, Contamination control

Abbreviations and Symbols

NPT	Normal pressure and temperature
RH	Relative humidity
dpi	Dots per inch
AFM	Atomic force microscope
QCM	Quartz crystal microbalance
TPCL	Three-phase contact line
CCR	Constant contact radius
CCA	Constant contact angle
std. dev.	Standard deviation
SEM	Scanning electron microscope
$\Delta\sigma$	Surface stress [$\mathrm{N\ m^{-1}}$]
Θ	Drop contact angle [°]
γ	Liquid surface tension [$\mathrm{N\ m^{-1}}$]
τ	Evaporation time [s]
η	Viscosity [mPa s]
ρ	Density [$\mathrm{g\ cm^3}$]
α	Thermal expansion coefficient [$\mathrm{K^{-1}}$]
v	Poisson's ratio
a	Drop contact radius [m]
m	Drop mass [kg]
g	Gravitational acceleration [$g = 9.8\,\mathrm{m\,s^{-2}}$]
f	Frequency [Hz]
k	Cantilever spring constant [N/m]
d	Cantilever thickness [m]
w	Cantilever width [m]
l_0	Cantilever length [m]
V	Drop volume [$\mathrm{m^3}$]
K	Capillary length [m]
ΔP	Laplace-, or capillary pressure [Pa]
P_0	Vapor pressure [Pa]
D	Diffusion coefficient [$\mathrm{cm^2\ s^{-1}}$]
T	Temperature [K]
E	Young's or elasticity modulus [Pa]
R	Drop radius of curvature [m]

2.1 Introduction

Understanding the kinetics of evaporation or drying of microscopic, sessile drops from solid surfaces is a key factor in a variety of technological processes, such as: (1) printing [1–3] and painting [4]; (2) heat-transfer applications, for example in the electronic industry to cool integrated circuits (ICs) and electronic components

[5–8], or for fire fighting [9]; (3) micro lithography, for example on polymer [10–13] or on biomaterial [14] surfaces. Such microscopic drops are primarily generated by spray nozzles and atomizers [15], or by inkjet devices and drop-on-demand generators [16]. Spray nozzles and atomizers are capable of simultaneously producing a large number of drops by one nozzle, but with a large size distribution and little control over the size (from below 1 μm to above 100 μm). The second type of apparatus is only capable of generating single consecutive drops by one nozzle, however monodisperse and with a good control over the size. In fact, the resolution of inkjet printers is steadily increasing as the size of the drops decreases. A commercial standard inkjet printer has nowadays a resolution of around 1,200 dpi, which means that the drops have a diameter of around 20 μm and a volume of around 4 pL. If such a drop would be pure water, instead of a mixture of water and dye, and be deposited on a flat surface, it would evaporate in less than 150 ms at normal pressure and temperature (NPT) and at a relative humidity (RH) of 50%. In comparison to inkjetted drops, rain drops have diameters between 1 and 2 mm, while drops in a fog have diameters below 10 μm [17].

Drop evaporation has been classically monitored by means of video-microscope imaging [18, 19], by ultra-precision weighing with electronic microbalances [20, 21] and with quartz crystal microbalances (QCM) [22]. Recently also atomic force microscope (AFM) cantilevers have been successfully employed for this purpose [23–25]. Using the first two, since long established techniques, a wealth of information was gained and the evaporation of macroscopic drops of simple liquids from inert surfaces is now well understood. These techniques are, however, not sensitive enough to characterize microscopic drops. Furthermore, they can not directly measure the interfacial stresses arising at the contact area between liquid and solid, which are known to play a key role in the evaporation kinetics of small drops [18, 20, 21, 26–28], nor are they capable of sensing the heat absorbed by the liquid during evaporation.

In this chapter evaporation studies of microscopic water drops on solid surfaces performed with a nonstandard technique are presented. It will be shown how it is possible to simultaneously measure surface forces, the mass, and the vaporization heat of a microdrop.

2.2 Background, Materials and Methods

2.2.1 Drop in Equilibrium

For the sake of simplicity, let us first consider a drop deposited onto a nondeformable and nonsoluble substrate (Fig. 2.1). In equilibrium, i.e. when the drop is not evaporating, Young's equation must hold. It establishes the relation among the three surface tensions acting at the rim of the drop (three-phase contact line, TPCL).

$$\gamma_S - \gamma_{SL} = \gamma_L \cos\Theta \tag{2.1}$$

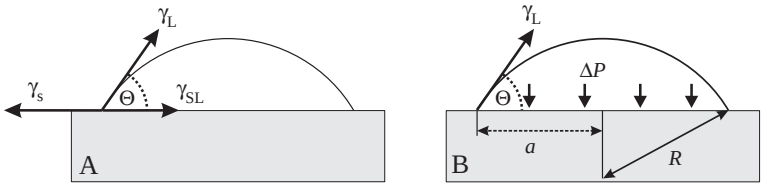

Fig. 2.1. (**A**) Sessile drop in equilibrium on a solid surface, with contact angle Θ and surface tensions γ_L, γ_S, and γ_{SL}. (**B**) Action of liquid surface tension γ_L and Laplace pressure ΔP

γ_L is the surface tension at the interface liquid/gas, γ_S is the surface tension at the interface solid/gas, and γ_{SL} is the surface tension at the interface solid/liquid. Θ is called contact angle, or wetting angle, of the liquid on the solid. Equation (2.1) is strictly valid only if the drop is not evaporating and if gravity can be neglected. We can neglect gravity, and thus the effect of the hydrostatic pressure that would flatten the drop, when the drop is smaller than the capillary length

$$K = \sqrt{\frac{\gamma_L}{\rho g}} \tag{2.2}$$

where ρ is the density of the liquid and g the gravitational acceleration. For water, $\gamma_L = 0.072\,\mathrm{N/m}$, $\rho = 1\,\mathrm{g/cm^3}$, and $g = 9.8\,\mathrm{m/s^2}$. The shape of the drop is thus not influenced by gravity if the radius of curvature is well below 2 mm. This requirement is fulfilled for all results presented in the following, where drops smaller than $100\,\mu\mathrm{m}$ were always used. For such sizes the shape of the drop is determined solely by surface forces and it has the form of a spherical cap.

In addition to the surface tensions acting at the TPCL, another force plays a major role. Because of its curvature, the pressure inside the drop is higher than outside. The difference between in and out is called Laplace or capillary pressure

$$\Delta P = \frac{2\gamma_L}{R} = \frac{2\gamma_L \sin\Theta}{a} \tag{2.3}$$

where R is the radius of curvature of the drop, which is related to the contact radius a and the contact angle Θ (Fig. 2.1).

As an example, for a drop of water forming a contact angle of 60° with a surface, the pressure difference is $\Delta P = 1.2\,\mathrm{mbar}$ when $a = 1\,\mathrm{mm}$, and $\Delta P = 1,200\,\mathrm{mbar}$ when $a = 1\,\mu\mathrm{m}$.

Summarizing, one can say that when a small, nonevaporating microdrop is sitting on a surface and forms a finite contact angle with it, the general picture is:

(1) The drop has a spherical shape.
(2) Young's equation accounts for the in plane (horizontal) balance of forces at the TPCL.
(3) The vertical component of the surface tension $\gamma_L \sin\Theta$ is pulling upwards at the TPCL and is counterbalanced by the Laplace pressure ΔP, which is pushing uniformly downwards over the whole contact area πa^2.

2.2.2 Evaporating Drop

Why do drops evaporate at all? A liquid (condensed phase) with a planar surface evaporates only when its vapor pressure P_0 is higher than the pressure of its vapor (gas phase) in its surroundings. As a consequence, if the surroundings are saturated with its vapor the liquid does not evaporate. It is in equilibrium, because at any time the number of molecules evaporating from and condensing to the surface is similar. However, drops have a slightly higher vapor pressure in comparison to a planar surface due to their curvature. For this reason, they evaporate also in a saturated atmosphere. This is quantified by the Kelvin Equation

$$P_V = P_0 \, e^{\lambda/R} \tag{2.4}$$

where the vapor pressure of the liquid in the drop is P_V, and the parameter λ is a function of the temperature and the nature of the liquid. Thus, the vapor pressure increases with decreasing drop size. As an example, a planar water surface has a vapor pressure $P_0 = 31.69\,\mathrm{mbar}$ at NPT. If the surface is curved and the radius of curvature is $R = 1\,\mu\mathrm{m}$, the vapor pressure is $P_V = 31.72\,\mathrm{mbar}$, and if $R = 100\,\mathrm{nm}$, $P_V = 32.02\,\mathrm{mbar}$. The difference between the planar and the curved surfaces is small, but high enough for the drop to evaporate.

The evaporation law for microscopic drops was derived for two cases for drops of pure liquids, assuming $\Theta = \mathrm{const}$ and neglecting the cooling resulting from the vaporization [29].

1. Drop in its saturated vapor

$$V_L = V_{L0} - \alpha D \cdot P_0 \cdot t \tag{2.5}$$

where V_L is the drop volume, V_{L0} is the initial drop volume, D is the diffusion coefficient of the molecules in the vapor, P_0 is the vapor pressure, and α is a known parameter that depends on the drop properties, on the contact angle, and on the temperature (for details see [29]). The equation contains no free parameters, and states that the volume of the drop decreases linearly with time.

2. Drop in nonsaturated vapor

$$V_L^{2/3} = V_{L0}^{2/3} - \beta \, D \cdot \varphi P_0 \cdot t \tag{2.6}$$

where φP_0, with $\varphi < 1$, represents the reduced vapor pressure, and β is a known parameter that depends on the drop properties, on the contact angle, and on the temperature. The equation contains no free parameters, and states that the volume of the drop to the power of 2/3 decreases linearly with time.

Both evaporation processes, in saturated and in nonsaturated atmosphere, are "diffusion limited", i.e. the evaporation is limited by the diffusion of the liquid molecules through a saturated vapor layer around the drop.

As an application of the above evaporation laws, the evaporation of microdrops of water with different initial volumina on a silicon surface coated with a 30-nm thick fluoropolymer film (perfluoro-1,3-dimethylcyclohexane) was observed. The initial contact angle was $\Theta = 90^\circ$ and remained constant for more than half of the evaporation time. During the experiments, the temperature ($\mathrm{T} = 25\,^\circ\mathrm{C}$) and the relative

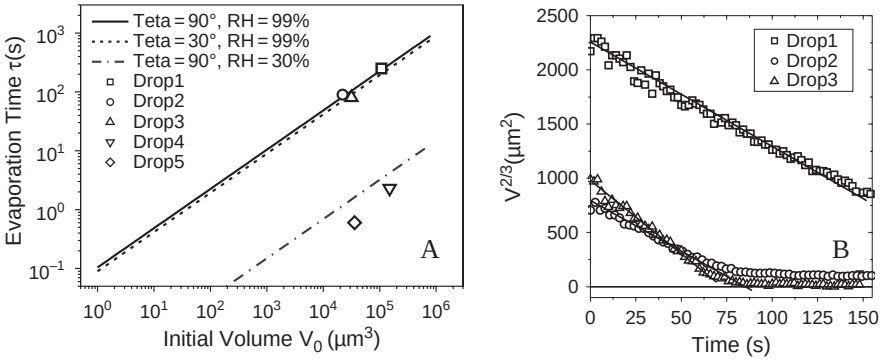

Fig. 2.2. (**A**) Calculated evaporation times τ versus initial drop volume V_0 for three cases: $\Theta = 90°$ and RH = 99% (*solid line*), $\Theta = 30°$ and RH = 99% (*dashed line*), and $\Theta = 90°$ and RH = 30% (*dashed-dotted line*). Corresponding experimental evaporation times (*open symbols*). (**B**) $V^{2/3}$ versus time for three drops; *solid lines* serve only as guides for the eye. (From [29])

humidity (RH $\sim$ 99%) were constant. The dimension of the evaporating drop was monitored from the side with a video microscope [23, 29].

Figure 2.2A shows the calculated evaporation times τ versus the initial drop volume V_0 (in double logarithmic scale), as calculated by Eq. (2.5) for RH = 99%. The similarity between the two upper lines, calculated for contact angles of $\Theta = 90°$ and 30°, emphasizes that τ depends more strongly on V_0 than on Θ. The slope of the curves is exactly 2/3. The first three hollow symbols represent evaporation times of microdrops with different initial volumina, all other parameters are unchanged. The agreement with the calculated times is very satisfying, especially since no free parameters were used. The model is also applicable for smaller RHs, as shown for two microdrops evaporating at RH = 30%: the calculations yield respectively $\tau = 4.3$ s and 1.6 s, the measurements yield $\tau = 2.2$ s and 0.6 s. The evaporation time is strongly dependent on the vapor saturation: at RH = 30% a microdrop with a mass of 150 ng evaporates in $\tau = 4.3$ s, at RH = 99% in $\tau = 290$ s, and at RH = 100% in $\tau = 7000$ s. It must be noted, that it is experimentally very difficult to set a constant RH = 100% for a prolonged time.

By representing $V^{2/3}$ versus time (Fig. 2.2B), the experiments reveal that at the beginning of the process, when the three evaporating drops are still large, the dependence is linear with time (solid lines). At the end of the process there are deviations and the evaporation appears to slow down. This can be due, for example to the presence of solid impurities in the water, which get enriched as the drop evaporates so that the vapor pressure decreases. Another explanation might be that the resolution limit of the optical technique is reached. In order to track the evaporation until the end an alternative technique will be introduced in the following paragraph. It will allow us to test the evaporation law also for extremely small drops.

2.2.3 Experimental Setup

When a drop is sitting on a surface, its surface tension pulls upwards at the TPCL, while the Laplace pressure pushes uniformly downwards on the entire contact area.

If the substrate is thin enough the surface forces can cause its bending: the thinner the plate, the stronger the bending. This can be used as a sensor principle. Silicon cantilevers, which look like microscopic diving boards, were employed as a suitable thin plate and a technique was developed for measuring the degree of cantilever bending. We employed silicon cantilevers like those imaged in Fig. 2.3A, where eight identical cantilevers are supported by a common silicon chip (Micromotive, Mainz, Germany). Nominal cantilever dimensions are: Length $l_0 = 750\,\mu\mathrm{m}$, width $w = 90\,\mu\mathrm{m}$, and thickness $d = 1\,\mu\mathrm{m}$. Using an inkjet capillary, water microdrops were deposited onto the upper side of a cantilever, close to its base (Fig. 2.3B). The working principle is as follows (Fig. 2.3C): (1) before drop deposition no forces act on the cantilever, which is thus straight (the effect of gravity induces a neglectable bending); (2) upon drop deposition the cantilever bends upwards. This bending can be measured with the so-called light lever technique, as usually done in AFM, where a laser beam is pointed at the free end of the cantilever; (3) the measured signal is not the "actual bending," but the "inclination" $\mathrm{d}z/\mathrm{d}x$ at the free end of the cantilever.

Simultaneously with cantilever inclination, a video microscope from the side records a movie of the evaporating drop from which the contact angle Θ and the contact radius a are calculated versus time. The width w of the cantilever needs to be at least two times larger than the contact radius a of the drop, i.e. if the drop touches the edges of the cantilever, border effects distort the shape of the drop, flawing the measurement of the contact angle. The experimental set-up used to deposit the microdrops onto the cantilever surface, monitor its inclination and resonance frequency and record the video of the evaporating drop is described in [23–26].

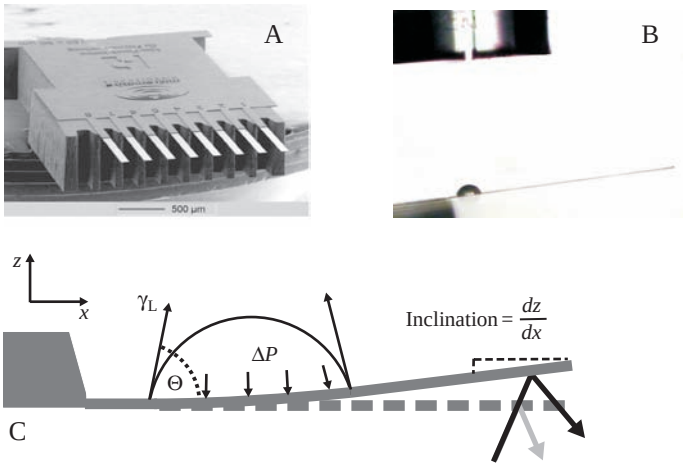

Fig. 2.3. (**A**) SEM image of a silicon chip with eight attached cantilevers. (**B**) Side view of a cantilever with drop deposited at its base and inkjet capillary used for drop generation. (**C**) Configuration of the equilibrium of forces between a drop and a cantilever: Θ is the equilibrium contact angle, γ_L is the liquid surface tension, ΔP is the Laplace pressure

2.3 Evaporation Results on Microdrops

2.3.1 Evaporation Curve

A typical evaporation curve of a water microdrop on a silicon cantilever, acquired at NPT and RH $\sim 30\%$, is a plot of the inclination of the cantilever versus time (Fig. 2.4A). At the same time, the contact angle Θ and the contact radius a can be recorded by video microscopy and plotted versus time (Fig. 2.4B, C). The water microdrop is deposited onto the cantilever at $t = 0$ with the inkjet device, and immediately starts to evaporate. The evaporation is accomplished after $\sim 0.6\,\mathrm{s}$, as the cantilever's inclination returns to its initial value. In the contact angle and contact radius curves, the black lines are simply guides for the eye. They show that two evaporation regimes take place: at the beginning, the drop evaporates in the Constant-Contact-Radius (CCR) mode, and after $\sim 0.3\,\mathrm{s}$ both, Θ and a, decrease linearly with time. Plots of V and of $V^{2/3}$ versus time demonstrate the agreement with the evaporation law derived in Eq. (2.6) for a drop evaporating in nonsaturated vapor.

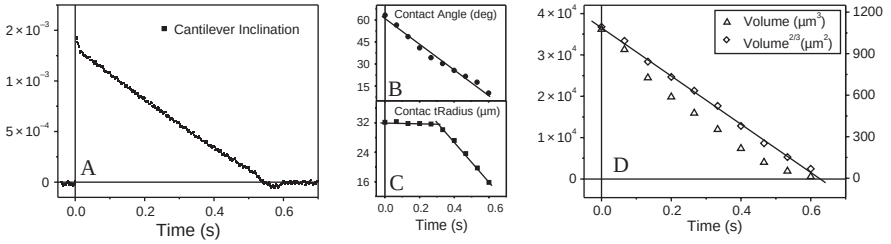

Fig. 2.4. $T \sim 25\,^{\circ}\mathrm{C}$, RH $\sim 30\%$; drop data: water, $a = 32\,\mu\mathrm{m}$, $\Theta = 63^{\circ}$, $\gamma_L = 0.072\,\mathrm{N/m}$, $m_0 = 36\,\mathrm{ng}$. Cantilever inclination (**A**), contact angle (**B**), contact radius (**C**), and volume and volume$^{2/3}$ versus time (**D**). *Solid lines* are guides for the eye

At this point a model is needed to analyze the acquired inclination data and relate it to surface forces, drop shape, and cantilever properties.

2.3.2 Force Model

First, for a simplified treatment, some assumptions on the drop and on the cantilever have to be made:

(1) The drop is in thermodynamic equilibrium, i.e. it does not evaporate, during the acquisition of a single data point. This is verified, since the acquisition time is typically $< 1\,\mathrm{ms}$.
(2) Beam theory is used for modeling the cantilever. It must hold $l_0 >> w$ and d, which means that the bending of the cantilever is considered to be one dimensional ($z = f(x)$) and that the transversal cross sections are flat. The Poisson's

ratio is zero ($\nu = 0$) in beam theory, which means that during its deformation the volume of the cantilever is not conserved.

The inclination at the end of the cantilever, which is given by the overall balance of forces acting on it, then is [23]:

$$\frac{dz}{dx} = \frac{3\pi a^3}{Ewd^3}\left[\gamma_L \sin\Theta + \frac{2d}{a}(\gamma_L \cos\Theta - \gamma_S + \gamma_{SL})\right] \tag{2.7}$$

where E is Young's modulus of the cantilever material, while all other parameters have been introduced before. The first term contains the vertical contribution of the surface tension and the Laplace pressure, while the second term is basically Young's equation. It is significant to note here that all parameters in this equation are known, i.e. there are no fitting parameters.

Figure 2.5 shows both the observed evaporation curve (Fig. 2.4A) and the curve calculated according to Eq. (2.7). The agreement between the two curves is fair, especially when considering that no fitting parameters were used and that the cantilever model is a simplification (Fig. 2.5).

It appears, however, that all curves acquired in similar experimental conditions lie systematically below the calculated curves. Thus, the model needs a refinement. According to the simplifications made, mainly three issues can cause this deviation:

(1) Beam theory was employed to model the cantilever and Poisson's ratio was zero ($\nu = 0$).
(2) The cantilever also has a lateral extension. Therefore a drop causes also a transversal bending of the cantilever, which increases its effective stiffness.
(3) The cantilever is clamped at the base. That edge can thus not be deformed, which increases its effective stiffness.

A more sophisticated 3D finite element (FE) model of the cantilever can be therefore implemented, which takes into account the above three issues [24]. In order to check the model the mechanical equilibrium deformation of a cantilever caused by a microdrop was analyzed. A nonevaporating ionic liquid (1-butyl-3-methylimidazolium hexafluorophosphate from Merck KGaA, Darmstadt,

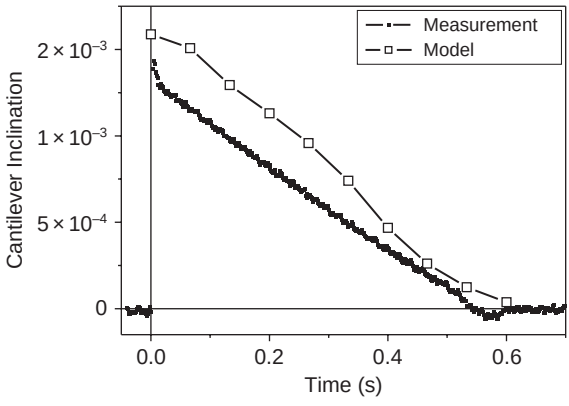

Fig. 2.5. T ∼ 25° C, RH ∼ 30%; drop data: water, $a = 32\,\mu\mathrm{m}$, $\Theta = 63°$, $\gamma_L = 0.072\,\mathrm{N/m}$, $m_0 = 36\,\mathrm{ng}$; cantilever data: silicon, $E = 180\,\mathrm{GPa}$, $l_0 = 500\,\mu\mathrm{m}$, $w = 100\,\mathrm{mm}$, $d = 0.9\,\mu\mathrm{m}$. Experimental and calculated curves in comparison. (From [23])

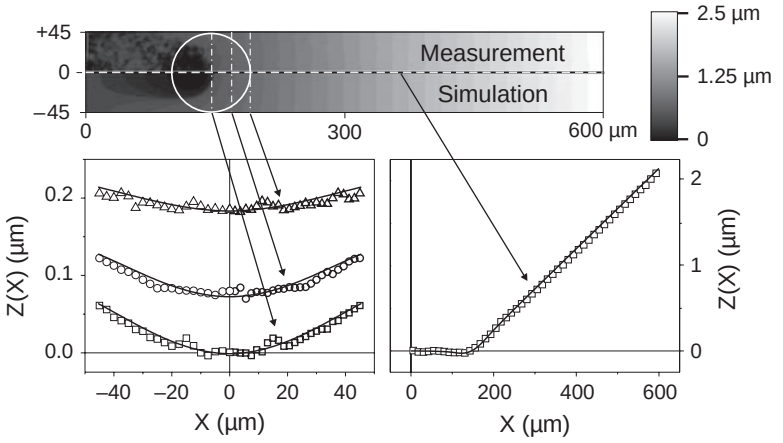

Fig. 2.6. Ionic liquid drop: $a = 45\,\mu\mathrm{m}$, $\Theta = 64°$, $\gamma_L = 0.045\,\mathrm{N/m}$; cantilever: $E = 180\,\mathrm{GPa}$, $v = 0.26$, $l_0 = 600\,\mu\mathrm{m}$, $w = 90\,\mathrm{mm}$, $d = 0.7\,\mu\mathrm{m}$. *Solid lines* represent simulations, *open symbols* experimental data points. (From [24])

Germany) was deposited onto a silicon cantilever. The face of the cantilever opposite to the one where the drop was sitting was imaged with a confocal profilometer (µ Surf from NanoFocus AG, Oberhausen, Germany) and a 3D image of the bent cantilever was obtained. It was then compared with the simulation results (Fig. 2.6)

A Young's modulus $E = 180\,\mathrm{GPa}$ and a Poisson's ratio $v = 0.26$, which are standard values for silicon, were used in the simulation. The upper half of Fig. 2.6 represents the measurement, the lower half the simulation, the white circle the position of the drop. The agreement between simulation and measurements is very satisfactory. In the lower left graph three transversal profiles of the cantilever, taken at the three places indicated by the arrows, are shown. Modeling this bending is beyond the capabilities of the analytic model. In the lower right graph the longitudinal profiles, experimental and simulated, are shown. The overall relative error is below 6% in this case, and below 10% on the average. This is an extremely good agreement, especially considering that all parameters of the simulation are fixed: they are determined from independent measurements (cantilever and drops dimensions) or are known from literature (silicon and ionic liquid properties).

From further parameter studies it resulted that the transversal bending and the clamping at the base cause negligible effects, so that the consideration of Poisson's ratio appears to be the dominating factor that causes the discrepancy between the analytic model and the experimental results [24].

2.3.3 Negative Inclination

Evaporation curves recorded with water drops deposited on very clean hydrophilic cantilevers systematically differ from curves recorded with drops on very clean hydrophobic cantilevers. Inclination and evaporation time have been normalized in

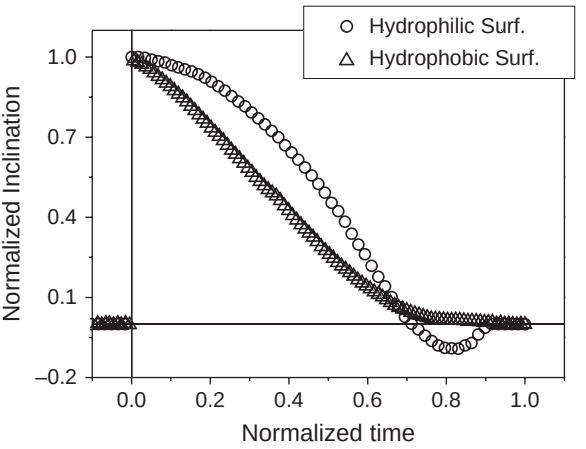

Fig. 2.7. Evaporation curves of two water microdrops on a cantilever with a hydrophilic (*blue circles*) and a hydrophobic (*red triangles*) surface. $T \sim 25\,^{\circ}C$, $RH \sim 30\%$. Hydrophilic case: $a = 37\,\mu m$, $\Theta = 70^{\circ}$, $m_0 = 66\,ng$. Hydrophobic case: $a = 34\,\mu m$, $\Theta = 116^{\circ}$, $m_0 = 187\,ng$

order to compare two measurements (Fig. 2.7). The difference is that the inclination becomes negative at the end of the "hydrophilic curve." This is not an artifact and is reproducible. The initial drop volumina were different, as well as the evaporation modi of the two drops. On the hydrophilic cantilever, the TPCL of the drop remained pinned for almost the entire evaporation, as far as could be concluded from video microscope images, while the contact angle of the drop gradually decreased. This corresponds to the CCR evaporation mode. Conversely, on the hydrophobic cantilever, both, contact radius and contact angle, changed during evaporation.

The negative inclination can not be explained by the model proposed before, because Eq. (2.7) contains only positive terms:

(1) The first is the contribution from the Laplace pressure ΔP and from the vertical component of the surface tension $\gamma_L \sin\Theta$.
(2) The second is basically Young's equation, which should be zero under the assumption that the drop is in thermodynamic quasi-equilibrium.

It is thus necessary to introduce an additional term, which must be negative and which describes the mechanical stress applied to the cantilever towards the end of evaporation of the drop. It can be called $\Delta\sigma$, for example, and one should keep in mind that it is not constant

$$\frac{dz}{dx} = \frac{3\pi a^3}{Ewd^3}\left[\gamma_L \sin\Theta + \frac{2d}{a}(\gamma_L \cos\Theta - \gamma_{SL} + \gamma_{SL}) + \Delta\sigma\right] \tag{2.8}$$

This additional stress is for now just a free parameter, which helps to describe the experimental curves. A tentative explanation of its physical origin could be as follows:

(1) When the contact angle is "large enough," the drop pulls at the TPCL and the cantilever bends upwards (Fig. 2.8A). The first term of the equation, $\gamma_L \sin\Theta$, dominates over the second term, $\gamma_L \cos\Theta - \gamma_{SL} + \gamma_{SL}$, which is zero under the

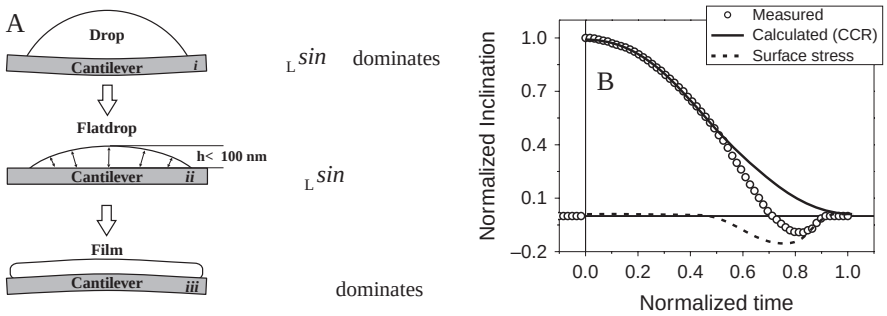

Fig. 2.8. (**A**) Schematic of the model to explain the negative cantilever inclination, and range of action of the forces involved. (**B**) Experimental evaporation curve (*circles*), calculated curve assuming CCR evaporation (*solid line*), and calculated surface stress (*dashed line*)

assumption of Young's equation being valid. The third term, $\Delta\sigma$, must also be negligible.

(2) When the drop becomes thinner than some 100 nm, the surface forces inside the flat drop start to play a role, favoring the formation of a thin film and acting to stabilize it. At this stage, ΔP, γ_L, and $\Delta\sigma$ have a similar magnitude and their effects on the bending of the cantilever cancel out each other. The cantilever crosses the "zero inclination" axis for the first time.

(3) Then, what is left of the drop wets the surface and forms a thin film, which could span a larger area than the original drop contact area. Now $\Delta\sigma$ dominates over the other two terms, which become vanishingly small. The interfacial tension between the water film and the cantilever is smaller than between air and the cantilever, so that the latter bends away from the drop. The measured signal is negative.

It may also be possible to determine $\Delta\sigma$ experimentally from the inclination curve (Fig. 2.8B). In fact, from video images it is known that the drop evaporates in the CCR mode. Assuming that the CCR mode holds until the end (last 100 ms), from the contact radius and contact angle data one could calculate the inclination as if only ΔP and γ_L were acting on the cantilever (solid line). Subtraction of these two curves yields the curve of $\Delta\sigma$ (dashed line). So, although measurable, still a quantitative description for $\Delta\sigma$ has to be found.

In summary, using cantilevers as sensors an effect arising with microscopic, pinned drops was observed which, to the best of our knowledge, was never observed using other methods. The tentative explanation is that a thin liquid film wets the surface, reduces the surface tension on the top side, and causes the cantilever to bend towards the bottom side.

2.3.4 Mass and Inclination

Surface forces exerted by the drop on the cantilever cause its bending. With the light lever technique the resulting inclination at the end of the cantilever is measured.

This signal can be called "static," since it changes continuously, but slowly, during the evaporation of the drop which takes usually one second. Additionally to this use, as surface stress sensors, cantilevers can also be employed as microbalances. Cantilevers are harmonic oscillators, whose resonance frequency depends, among other parameters, on their own mass and on their load. The change of the resonance frequency caused by the mass change of the evaporating drop can be recorded. This signal can be called "dynamic" with respect to the "static" signal described before, because a cantilever oscillation takes less than a millisecond.

Assuming that Young's equation is valid at all times, that the additional surface stress $\Delta\sigma$ is negligible, and that the evaporation takes place in the CCA mode (these issues are practically met using a hydrophobized cantilever), the "static" equation simplifies to

$$\frac{dz}{dx} \approx \frac{3\pi a^3}{Ewd^3}\gamma \sin\Theta \tag{2.9}$$

while the "dynamic" equation states that the mass added to the cantilever (load) is inversely proportional to the resonance frequency squared [25, 30].

$$m \propto \frac{1}{(2\pi f)^2} \tag{2.10}$$

The two signals, inclination and resonance frequency, are acquired simultaneously, but are independent of each other. They yield the stress and the mass (Fig. 2.9). As an example of a simultaneous static and dynamic signal analysis, a water drop was deposited onto a silicon cantilever hydrophobized with a monolayer of hexamethyldisilazane (HMDS). The initial contact angle was $\sim 80°$. It decreased nearly linearly during evaporation, and was $\sim 70°$ at the end. The initial contact radius was $\sim 33\,\mu\mathrm{m}$, and decreased nearly linearly during evaporation. At the end it was below $10\,\mu\mathrm{m}$. At present, we can record the inclination curve with a temporal resolution of $\sim 0.1\,\mathrm{ms}$ between data points, and the frequency curve with $\sim 5\,\mathrm{ms}$. The mass calculated from the resonance frequency of the cantilever and from video

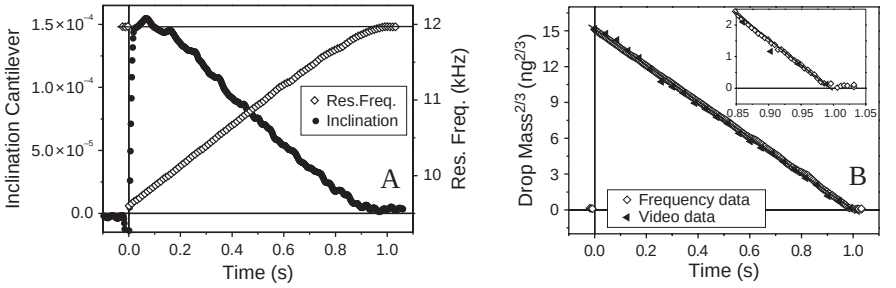

Fig. 2.9. (**A**) Simultaneously acquired inclination (*blue full circles*) and resonance frequency (*red hollow diamonds*) of a cantilever versus time upon evaporation of a water microdrop on a hydrophobized silicon cantilever. T $\sim 25\,°\mathrm{C}$, RH $\sim 30\%$. Drop data: $a = 33\,\mu\mathrm{m}, \Theta = 80°$, $\gamma_L = 0.072\,\mathrm{N/m}$, $m_0 = 60\,\mathrm{ng}$. Cantilever data: $l_0 = 500\,\mu\mathrm{m}$, $w = 90\,\mu\mathrm{m}$, $d = 2.1\,\mu\mathrm{m}$. (**B**) Drop mass$^{2/3}$ versus time from frequency (*hollow diamonds*) and video (*black triangles*) data, and linear fit (*solid line*)

microscope images is similar (Fig. 2.9B), although the time resolution ($\sim 5\,\mathrm{ms}$) and the sensitivity ($\sim 50\,\mathrm{pg}$) is much higher for the frequency-derived mass. This offers the possibility of studying drop evaporation closer to its end (see inset). If the mass is plotted as "$m^{2/3}$ versus time" it results that the evaporation law "$V^{2/3}$ linear vs. time," which is valid for macroscopic drops, can be extended to microscopic drops and is valid until the evaporation ends.

In summary, using cantilevers as drop evaporation sensors we can simultaneously record the mass of the drop by tracking the resonance frequency of the cantilever, and the surface forces of the drop by tracking the inclination of the cantilever.

2.3.5 Vaporization Heat

Upon evaporation, a drop absorbs heat from its surroundings (air and cantilever). For example, a water drop cools down by 1–2 °C [31], while benzene cools down by 15–20 °C [32]. The processes involved in heat dissipation in this case are mainly conduction and convection. If the cantilever is made of pure, crystalline silicon, the cooling does not affect its bending, as shown in Fig. 2.10A [33]. The cantilever inclination measured upon deposition of a microdrop of water, which is the result of the combined action of surface forces and thermal effect, and the inclination simulated taking into account the surface forces only, from Eq. (2.7), are in good agreement. The difference between the two curves is smaller than 10% over all the evaporation.

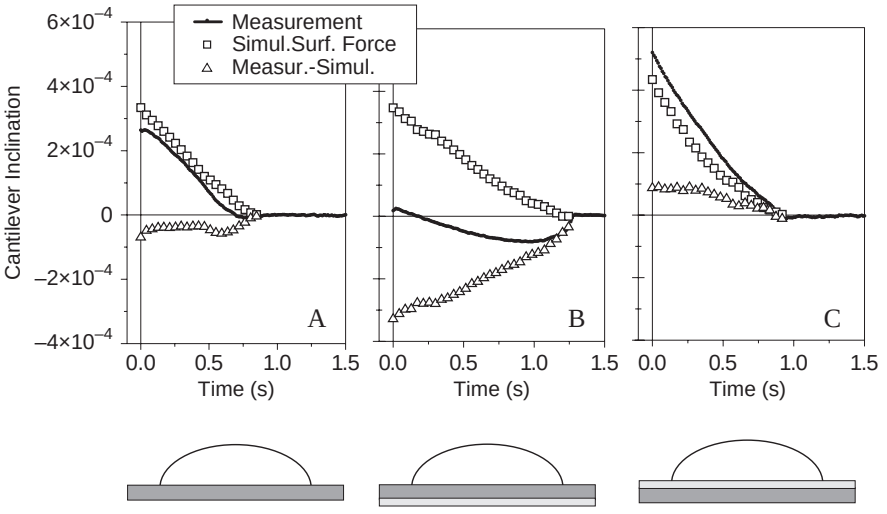

Fig. 2.10. Experimental (*solid line*), simulated (*hollow squares*), and difference (*hollow triangles*) inclination of silicon cantilevers versus time upon evaporation of water microdrops. $T \sim 25\,^{\circ}\mathrm{C}, RH \sim 30\%$. Drop data: various initial volumes, contact radii, and contact angles; $\gamma_L = 0.072\,\mathrm{N/m}$. Cantilever data: $l_0 = 750\,\mu\mathrm{m}$, $w = 90\,\mu\mathrm{m}$, $d_A = 1.8\,\mu\mathrm{m}$, $d_B = 1.5\,\mu\mathrm{m}$, and $d_C = 1.7\,\mu\mathrm{m}$; Gold layer thickness $= 30\,\mathrm{nm}$; Young's Moduli: $E_{Si} = 180\,\mathrm{GPa}$, $E_{Au} = 78\,\mathrm{GPa}$; Poisson's ratios: $\nu_{Si} = 0.26$, $\nu_{Au} = 0.44$

However, if the cantilever is, for example, gold coated on one of its sides, it behaves like a bimetal, since silicon and gold have different linear thermal expansion coefficients of $\alpha_{Si} = 2.6 \times 10^{-6}\,\mathrm{K}^{-1}$ and $\alpha_{Au} = 14.2 \times 10^{-6}\,\mathrm{K}^{-1}$, respectively. The direction of the bending depends on which side the gold layer is with respect to the drop. The thermal effect alone (experimental inclination minus inclination simulated for surface forces) would cause the cantilever to bend downwards (negative inclination) if the gold layer is on the bottom (Fig. 2.10B), or upwards (positive inclination) if the gold layer is on the top (Fig. 2.10C). The three water drops used here had different initial volumina, and the three cantilevers had different thicknesses. The evaporation times and the inclinations are therefore not directly comparable. However, contact angle and radius of each drop were recorded during evaporation, and the cantilever properties are known. With these data FE simulations were performed.

In summary, with the proper choice of the cantilever coating it is possible to sense the temperature of the evaporating drop, along with its mass and the effect of its surface tension.

2.4 Further Applications of Drops on Cantilevers

2.4.1 Spring Constant Calibration

The calibration of the spring constant of cantilevers is a fundamental issue in all AFM applications that involve force measurements [34, 35]. If cantilevers are employed to determine surface forces, a quantitative statement is possible only when the spring or force constant of the cantilever is known. The spring constant of commercially available cantilevers lies between $k \approx 0.01$ and $k \approx 50\,\mathrm{N/m}$. "Soft" cantilevers with k between 0.01 and 1 N/m are usually employed for the measurements of surface forces like adhesion, van der Waals interactions, and electrostatic forces. Because of their small spring constant, they allow for a high force resolution. "Stiff" cantilevers are commonly used for indentation measurements and nanolithography [34, 35] on soft samples, and for imaging in tapping mode. In the last 15 years a variety of methods have been introduced for the experimental determination of spring constants. Out of them all, around four methods have been established as standards [36, 37]. The first method makes use of the dimensions and the material properties of the cantilever, as well as its experimental resonance frequency and the quality factor of the resonance spectrum [38–45]. This approach is suited for rectangular cantilevers with known dimensions, for which it provides accurate results (std. dev. $< 10\%$). The second method is based on the acquisition of the thermal noise spectrum of the cantilever [46,47]. It is referred to as the "thermal noise method." It can be applied to cantilevers of any shape and does not require precise measurements of the cantilever dimensions, but suffers from a disadvantage: at least one force curve has to be acquired with the cantilever on a hard substrate in order to calibrate the spectrum. This can contaminate or damage the tip. The results obtained by this method are also accurate and

reproducible (std. dev. $< 10\%$). The third method is a so-called "direct" method. A known force is applied to the cantilever and the resulting bending is measured with the light lever technique. This force can be of hydrodynamic origin and act along [48–50] or at the free end [51] of the cantilever. The force can also be exerted by a second cantilever with a known spring constant [52, 53], by electrostatics [54], or by excitation with microdrops of known mass and velocity [23]. For all these techniques, special instruments need to be developed. Further, contamination of the tip or of the surface of the cantilevers is possible. The results obtained by this method are usually a little less accurate (std. dev. $< 15\%$). The fourth method, and also the most used/cited according to ISI – Web of Science^{SM}, was presented by Cleveland et al. [30]. It provides extremely precise values (std. dev. $\sim 5\%$). A cantilever is loaded at known positions with small weights (in the nanogram range) and the resulting shift of the resonance frequency is measured [see Eq. (2.10)]. This method, also referred to as the "added mass method," can be applied to all types of cantilevers and has no major restrictions. However, it is somehow time consuming:

(1) weights or particles of different masses must be placed at the very free end of the cantilever without damaging it
(2) the thermal noise spectrum must be acquired for each particle
(3) the particles must be removed without damaging the cantilever, and be positioned on a sample holder for having later their dimensions characterized by a SEM to calculate their mass.

This last technique can be refined and simplified [25]. Instead of weights, microdrops have been used. The method has two advantages: first, contamination is avoided by working "contactless." Water drops are generated and deposited on the cantilever surface by a XYZ-controlled inkjet nozzle; second, since the drops evaporate after some time, the weight does not need to be removed manually.

The technique has been validated in two ways:

(1) Microdrops with different masses were deposited at the free end of a cantilever (similar to the "added mass method") and the resonance frequency of the cantilever was measured. It is not necessary any more to acquire a thermal noise spectrum, because the cantilever is excited by the drop impact and oscillates with an amplitude. The result was compared to results from beam theory, and the spring constant was calculated according to Eq. (2.10) (Fig. 2.11A). This can be done because the cantilever with the drop at its end is a harmonic oscillator, and for the dependence of its resonance from the drop mass a closed solution does exist.
(2) Microdrops with similar mass were deposited at different positions along a cantilever, the resonance frequency was measured for each drop, the result was compared to predictions from FE simulations, and the spring constants were calculated (Fig. 2.11B). FE simulations are necessary because the system with the drop along the cantilever is still a harmonic oscillator, but the dependence of its frequency from the drop mass does not have an analytic solution.

The obtained values are in good agreement with calibration results of the same cantilevers obtained by the "thermal noise method" (TN) (Table 2.1).

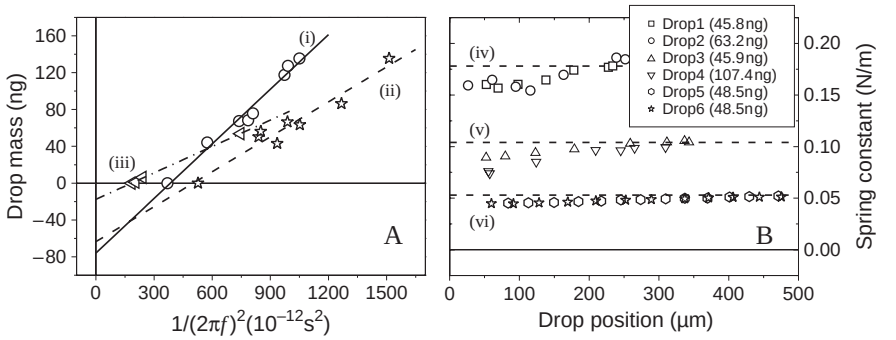

Fig. 2.11. (**A**) Mass of different water drops versus $1/(2\pi f)^2$ for three cantilevers. (i) Rectangular cantilever: $l_0 = 500\,\mu\mathrm{m}$, $w = 90\,\mu\mathrm{m}$. The linear regression of the data yields $k \approx 0.198\,\mathrm{N/m}$. (ii) Rectangular cantilever: $l_0 = 460\,\mu\mathrm{m}$, $w = 50\,\mu\mathrm{m}$. $k \approx 0.126\,\mathrm{N/m}$. (iii) Triangular cantilever: $l_0 = 200\,\mu\mathrm{m}$, $w = 22\,\mu\mathrm{m}$. $k \approx 0.096\,\mathrm{N/m}$. (**B**) Spring constants versus drop position for the rectangular cantilevers (iv), (v), and (vi). The *dashed horizontal line* represents the results from the "thermal noise method". (From [25])

Table 2.1. Values of the spring constant, calibrated by the thermal noise method (TN) and by the microdrops (EXP), for six different commercial cantilevers, with different dimensions and by different manufacturers

Cantilever	l_0 [μm]	f_0 [Hz]	K_{TN} [N/m]	Nr. of drops	K_{EXP} [N/m]	E_{rel}[%] $(K_{\mathrm{TN}} - K_{\mathrm{EXP}})/K_{\mathrm{TN}}$
(i) Micromotive, rectangular	500	10,404	0.19 ± 0.01	7	0.198 ± 0.012	4.2
(ii) Nanosensors, rectangular	460	11,782	0.13 ± 0.01	7	0.126 ± 0.012	3.1
(iii) Veeco, triangular	200	19,253	0.10 ± 0.01	3	0.096 ± 0.002	4.0
(iv) Micromotive, rectangular	297	16,900	0.178 ± 0.01	2×8	0.170 ± 0.010	4.5
(v) Micromotive, rectangular	372	11,215	0.104 ± 0.01	2×7	0.098 ± 0.006	5.8
(vi) Micromotive, rectangular	503	6,400	0.053 ± 0.01	2×12	0.048 ± 0.002	9.4

2.4.2 Contamination Control of Cantilevers

The resolution of AFM imaging strongly depends on the shape and chemical composition of the cantilever tip. Scanning a surface with a double-tip results in an image with a so-called "ghost." Scanning a surface with a contaminated tip results in a large adhesion between tip and sample, which increases the contact area and

decreases the resolution [55]. AFM is not only used for imaging, but also for friction measurements [56–59], surface force measurements in air or liquids [60, 61], force spectroscopy between biomolecules [62–66], and adhesion [67, 68], just to cite a few. Reliable and reproducible results can be obtained only with a clean, or at least known, AFM tip chemistry. Cleanliness is also important for the quality of further surface modifications of the AFM tip. Thin layers of contaminants may change the reactivity or adsorptivity of its surface. Also cantilevers without tips are used as force transducers and micromechanical stress sensors [69–72], above all for biochemical applications. In this case the whole cantilever must be chemically modified and/or functionalized. For this, a noncontaminated surface is required. Because the AFM tip is so small, characterization of its surface chemistry is difficult. One indirect approach is to characterize a reference surface that is made of the same material as the AFM tip and treated with the same process as the tip, by means of macroscopic techniques. Contact angle measurements [73] or X-ray photoelectron spectroscopy (XPS) [74] are often employed. However, unless the reference surface was subjected to the same storage conditions, it might not be representative of the cantilever and tip surface chemistry. Surface sensitive methods, like scanning Auger microscopy (SAM [75]) and time-of-flight secondary-ion mass spectroscopy (TOF-SIMS [74]), have been employed to perform surface microarea analyses (areas of hundreds of square micrometers) on the cantilevers. These methods allow for a precise characterization of the contaminants, however they do not allow for the characterization of the sole tip area, and are indeed time consuming and expensive. A simple and straightforward method for checking tip contamination was proposed by Thundat et al. [55]: by monitoring the change of the adhesion between tip and sample during imaging one can infer the degree of contamination.

Several procedures for cleaning the AFM tip-cantilever assembly have been discussed in the literature. Such procedures include ultraviolet ozone treatment [75, 76], aggressive acid-based baths [63, 74] and plasma etching [66, 77]. The majority of AFM users directly use as-received cantilevers, or they simply clean them by rinsing with organic solvents. This demonstrates that despite the fact that the AFM community has grown in the last years, apparently contamination is still considered a minor issue. Earlier attempts to draw attention to it reported that contamination undoubtedly affects AFM experiments [55], and that the main source of organic contamination on new cantilevers comes from their packaging [74]. To simplify the characterization avoiding the use of such expensive apparatus cited above, a straightforward, low-cost, and effective way of characterizing the wetting behavior of cantilevers and tips was proposed [78]. A small water drop is deposited directly on the cantilever by an inkjet nozzle. On deposition, the drop spreads depending on the hydrophobicity (contact angle) of the cantilever surface, and finally attains a contact radius a and a contact angle Θ. They are determined by video microscopy (Fig. 2.12).

One of the most used rectangular contact mode cantilevers, the Pointprobe (Nanosensors, Neuchatel, Switzerland), with a length $l_0 = 470\,\mu\mathrm{m}$, a width $w = 50\,\mu\mathrm{m}$, and a thickness $d = 2\,\mu\mathrm{m}$ was examined. The average contact angle of a water microdrop on an as-received cantilever was $\Theta \approx 88^\circ$ ($\pm 1^\circ$) (Fig. 2.12A). After cleaning in a plasma reactor (PDC-002, Harrick Scientific Corp., NY) under an argon atmosphere at medium power over 20 s, the contact angle decreased to $\Theta \approx 11^\circ$ ($\pm 2^\circ$). Since the drop strongly wets the surface, the drop shape is not

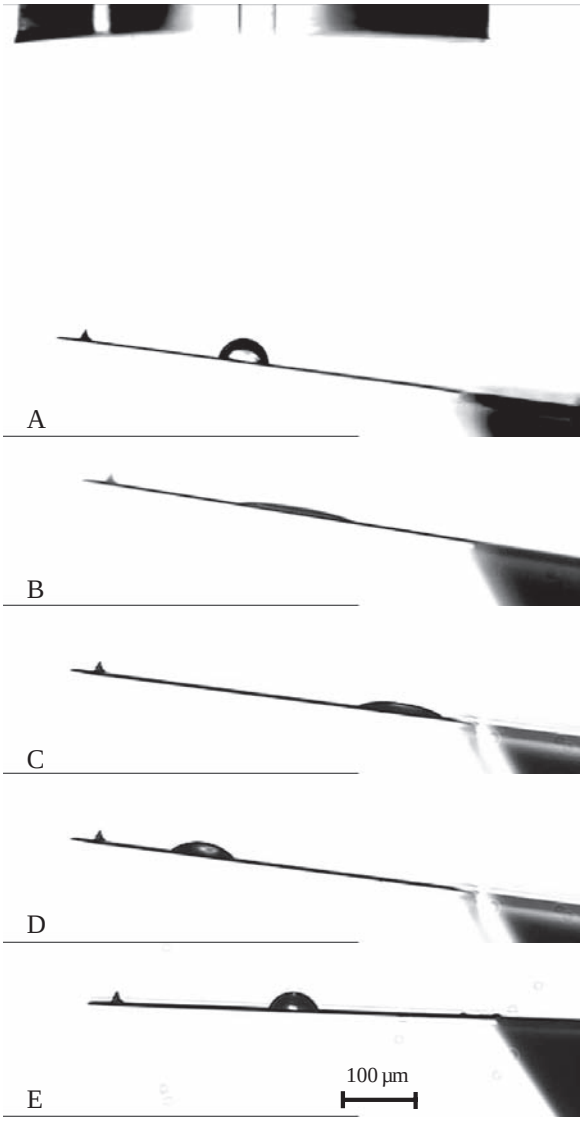

Fig. 2.12. Sequence of five images of water microdrops on a rectangular silicon cantilever. Before plasma cleaning (**A**) the drop forms a contact angle $\Theta = 88° \ (\pm 1°)$; after plasma cleaning (**B**) the contact angle is $\Theta = 11° \ (\pm 2°)$; after storage of the cantilever in a Gel-Box® for 1 (**C**), 3 (**D**) and 24 (**E**) hours, the drop forms contact angles of $\Theta = 26° \ (\pm 2°)$, $45° \ (\pm 3°)$, and $72° \ (\pm 3°)$. (From [78])

spherical anymore (Fig. 2.12B). The recontamination was controlled by storing the cantilever in a Gel-Box® (Gel-Pak Inc., Hayward, CA) for different long periods of time. Micro contact angle measurements were performed after 1, 3, and 24 hours (Fig. 2.12C–E). The contact angle increased stepwise, and after 24 hours was $\Theta \approx 72° (\pm 3°)$. On the basis of these results can be concluded that plasma cleaning removes satisfactorily the silicone oil contamination. However, cleaned cantilevers are fully recontaminated if they are stored in plastic boxes for 24 hours.

2.5 Conclusions

Drop evaporation has been commonly observed by means of video-microscope imaging and ultra-precision weighing with electronic microbalances or with quartz crystal microbalances. Abundant information was gained over the years with these techniques, so that the evaporation of macroscopic drops of simple liquids from inert surfaces is nowadays well understood. The same techniques are, however, not applicable to microscopic drops. Furthermore, they do not directly provide a measure of the interfacial stresses arising at the contact area between liquid and solid, which are known to play a key role in the evaporation kinetics of small drops. It was shown that atomic force microscope (AFM) cantilevers can be used as sensitive stress, mass, and temperature sensors, and how they can be employed to monitor the evaporation of microdrops of water from solid surfaces. The technique has some advantages with respect to state-of-the-art techniques cited above, since it allows one to measure more drop parameters simultaneously and for smaller drop sizes. The technique further allows detection of differences between water microdrops evaporating from clean hydrophilic and hydrophobic surfaces. The difference is especially manifest close to the end of evaporation. The evidence arises that on the hydrophilic surface a thin water film forms, while this is not the case for the hydrophobic surface. Metal-coated cantilevers can be used as thermometers, and allow one to precisely measure the temperature of an evaporating microdrop. This can be relevant for further applications of cantilevers as micro-sized calorimetric sensors for chemical reactions taking place in drops on their surface.

Further applications of the inkjet technology combined with cantilever sensors allows one to test the local cleanliness of cantilever surfaces with micro contact angle measurements, or to calibrate the spring constant of cantilevers in a contactless and noncontaminating way.

Acknowledgments. E.B. acknowledges the Max pLanck Society (MPG) for financial support. This work was partially funded by the German Research Foundation (DFG) (Forschergruppe FOR 516, WI 1705/7).

References

1. Heilmann J, Lindqvist U (2000) J Imag Sci Technol 44:491
2. Socol Y, Berenstein L, Melamed O, Zaban A, Nitzan B (2004) J Imag Sci Technol 48:15

3. Kim EK, Ekerdt JG, Willson CG (2005) J Vac Sci Technol B 23:1515
4. Tullo AH (2002) Chem Eng News 80:27
5. Chou FC, Gong SC, Chung CR, Wang MW, Chang CY (2004) Jap J Appl Phys 1 43:5609
6. Fabbri M, Jiang SJ, Dhir VK (2005) J Heat Mass Transf 127:38
7. Amon CH, Yao SC, Wu CF, Hsieh CC (2005) J Heat Transf Trans ASME 127:66
8. Shedd TA (2007) Heat Transf Eng 28:87
9. "Fogtech International". www.fogtec-international.com
10. Kawase T, Sirringhaus H, Friend RH, Shimoda T (2001) Adv Mater 13:1601
11. Bonaccurso E, Butt HJ, Hankeln B, Niesenhaus B, Graf K (2005) Appl Phys Lett 86:124101
12. de Gans BJ, Hoeppener S, Schubert US (2006) Adv Mater 18:910
13. Karabasheva S, Baluschev S, Graf K (2006) Appl Phys Lett 89:031110
14. Ionescu RE, Marks RS, Gheber LA (2003) Nano Letters 3:1639
15. Lefebvre AH (1989) Atomization and Sprays. Taylor & Francis
16. Lee ER (2003) Microdrop Generation. CRC Press, Taylor and Francis
17. Edwards BF, Wilder JW, Scime EE (2001) Eur J Phys 22:113
18. Bourges-Monnier C, Shanahan MER (1995) Langmuir 11:2820
19. Rowan SM, Newton MI, McHale G (1995) J Phys Chem 99:13268
20. Birdi KS, Vu DT, Winter A (1989) J Phys Chem 93:3702
21. Picknett RG, Bexon R (1977) J Colloid Interface Sci 61:336
22. Pham NT, McHale G, Newton MI, Carroll BJ, Rowan SM (2004) Langmuir 20:841
23. Bonaccurso E, Butt HJ (2005) J Phys Chem B 109:253
24. Haschke T, Bonaccurso E, Butt H-J, Lautenschlager D, Schönfeld F, Wiechert W (2006) J Micromech Microeng 16:2273
25. Golovko DS, Haschke T, Wiechert W, Bonaccurso E (2007) Rev Sci Instrum 78:043705
26. Obrien RN, Saville P (1987) Langmuir 3:41
27. Cordeiro RM, Pakula T (2005) J Phys Chem B 109:4152
28. Soolaman DM, Yu HZ (2005) J Phys Chem B 109:17967
29. Butt HJ, Golovko DS, Bonaccurso E (2007) J Phys Chem B 111:5277
30. Cleveland JP, Manne S, Bocek D, Hansma PK (1993) Rev Sci Instrum 64:403
31. David S, Sefiane K, Tadrist L (2007) Colloid Surf A 298:108
32. Blinov VI, Dobrynina VV (1971) J Eng Phys Thermophys 21:229
33. Golovko DS, Bonanno P, Lorenzoni S, Raiteri R, Bonaccurso E (2008) J Micromech Microeng 18:095026
34. Butt HJ, Cappella B, Kappl M (2005) Surface Science Reports 59:1–152
35. Cappella B, Dietler G (1999) Surf Sci Rep 34:1
36. Burnham NA, Chen X, Hodges CS, Matei GA, Thoreson EJ, Roberts CJ, Davies MC, Tendler SJB (2003) Nanotechnology 14:1
37. Ralston J, Larson I, Rutland MW, Feiler AA, Kleijn M (2005) Pure Appl Chem 77:2149
38. Green CP, Lioe H, Cleveland JP, Proksch R, Mulvaney P, Sader JE (2004) Rev Sci Instrum 75:1988
39. Green CP, Sader JE (2002) J Appl Phys 92:6262
40. Green CP, Sader JE (2005) J Appl Phys 98:114913
41. Green CP, Sader JE (2005) Phys Fluids 17:073102
42. Higgins MJ, Proksch R, Sader JE, Polcik M, Mc Endoo S, Cleveland JP, Jarvis SP (2006) Rev Sci Instrum 77:013701
43. Sader JE (1998) J Appl Phys 84:64
44. Sader JE, Chon JWM, Mulvaney P (1999) Rev Sci Instrum 70:3967
45. Sader JE, Larson I, Mulvaney P, White LR (1995) Rev Sci Instrum 66:3789
46. Butt H-J, Jaschke M (1995) Nanotechnology 6:1
47. Hutter JL, Bechhoefer J (1993) Rev Sci Instrum 64:1868
48. Craig VSJ, Neto C (2001) Langmuir 17:6018

49. Notley SM, Biggs S, Craig VSJ (2003) Rev Sci Instrum 74:4026
50. Senden TJ, Ducker WA (1994) Langmuir 10:1003
51. Maeda N, Senden TJ (2000) Langmuir 16:9282
52. Torii A, Sasaki M, Hane K, Okuma S (1996) Meas Sci Technol 7:179
53. Tortonese M, Kirk M (1997) SPIE Proc 3009:53
54. Bonaccurso E, Schonfeld F, Butt HJ (2006) Phys Rev B 74:085413
55. Thundat T, Zheng X-Y, Chen GY, Sharp SL, Warmack RJ (1993) Appl Phys Lett 63:2150
56. Mate CM, McClelland GM, Erlandsson R, Chiang S (1987) Phys Rev Lett 59:1942
57. Marti O, Colchero J, Mlynek J (1990) Nanotechnology 1:141
58. Meyer E, Lüthi R, Howald L, MBammerlin M, Guggisberg M, Güntherodt H-J (1996) J Vac Sci Technol B 14:1285
59. Tsukruk VV, Bliznyuk VN (1998) Langmuir 14:446
60. Butt H-J (1991) Biophys J 60:1438
61. Ducker WA, Senden TJ, Pashley RM (1991) Nature 353:239
62. Florin E-L, Moy VT, Gaub HE (1994) Science 264:415
63. Hinterdorfer P, Baumgartner W, Gruber HJ, Schilcher K, Schindler H (1996) Proc Nat Acad Sci USA 93:3477
64. Radmacher M (1999) Physics World 12:33
65. Heinz WF, Hoh J (1999) Nanotechnology 17:143
66. Lee GU, Kidwell DA, Colton RJ (1994) Langmuir 10:354
67. Hoh J, Cleveland JP, Prater CB, Revel J-P, Hansma PK (1992) J Am Chem Soc 114:4917
68. Heim L-O, Blum J, Preuss M, Butt H-J (1999) Phys Rev Lett 83:3328
69. Berger R, Gerber C, Lang HP, Gimzewski JK (1997) Microel Eng 35:373
70. Fritz J, Baller MK, Lang HP, Rothuizen H, Vettiger P, Meyer E, Güntherodt H-J, Gerber C, Gimzewski JK (2000) Science 288:316
71. Raiteri R, Grattarola M, Butt H-J, Skladal P (2001) Sens Actuators B 79:115
72. Lang HP, Hegner M, Meyer E, Gerber C (2002) Nanotechnology 13:R29
73. Knapp HF, Stemmer A (1999) Surf Interface Anal 27:324
74. Lo Y, Huefner ND, Chan WS, Dryden P, Hagenhoff B, Beebe TP (1999) Langmuir 15:6522
75. Arai T, Tomitori M (1998) Appl Phys A 66:S319
76. Fujihira M, Okabe Y, Tani Y, Furugori M, Akiba U (2000) Ultramicroscopy 82:181
77. Senden TJ, Drummond CJ (1995) Coll Surf A: Physicochem Eng Asp 94:29
78. Bonaccurso E, Gillies G (2004) Langmuir 20:11824